Available online at www.sciencedirect.com
SCIENCE DIRECT
Journal of Power Sources 158 (2006) 765–772
JOURNAL OF POWER SOURCES
www.elsevier.com/locate/jpowsour

Effect of pore size and surface area of carbide derived carbons on specific capacitance

J. Chmiola, G. Yushin, R. Dash, Y. Gogotsi *

A.J. Drexel Nanotechnology Institute and Department of Materials Science and Engineering, Drexel University, 3141 Chestnut St, Philadelphia, PA 19104, USA

Received 2 August 2005; received in revised form 6 September 2005; accepted 8 September 2005
Available online 19 October 2005

Abstract

This work presents a systematic study on how pore size and specific surface area (SSA) of carbon effect specific capacitance and frequency response behavior. Carbide derived carbons (CDC) produced by leaching metals from TiC and ZrC at temperatures from 600 to 1200 °C have highly tailorable microstructure and porosity, allowing them to serve as excellent model systems for porous carbons in general. BET SSA and average pore size increased with synthesis temperature and was 600–2000 $m^2 g^{-1}$ and 0.7–1.85 nm, respectively. Maximum specific capacitance in 1 M H_2SO_4 was found to occur at an intermediate synthesis temperature, 800 °C, for both ZrC and TiC derived carbons and was 190 and 150 F g^{-1}, respectively. Volumetric capacitance for TiC and ZrC derived carbons was maximum at 140 and 110 F cm^{-3}. These results contradict an oft-reported axiom that increasing pore size and SSA, all other things being held constant, increases specific capacitance. A correlation between specific capacitance and SSA of micropores (less than 2 nm in diameter) has been shown. As expected, increasing pore size was found to improve the frequency response. However, CDCs with similar pore size distributions but obtained from different starting materials showed noticeable differences in impedance behavior. This highlights the importance of not only the pore size and specific surface area measured using gas sorption techniques, but also the pore shape or tortuousity, which is non-trivial to characterize, on energy storage.

Keywords: Supercapacitor; Power device; Electrochemical capacitor; Carbide derived carbon

1. Introduction

With increasing demand for high power electronic devices with an ever-decreasing size, supercapacitors have begun filling the niche between electrochemical batteries and dielectric capacitors [1–3]. Supercapacitors, with the pioneering work occurring nearly 50 years ago with a patent granted to Becker [4], have shown promise to fill this apparent contradiction between the explosive growth of power required by devices and the lack of growth in the energy storage devices supplying them.

Supercapacitors use electrostatic ion adsorption on the electrolyte/electrode double-layer interfaces of porous carbons with specific surface areas typically in the range of 1000–3000 $m^2 g^{-1}$ to store electrical energy [5]. Because there are no charge-transfer reactions occurring during the charge–discharge process, these devices avoid many of the pitfalls of conventional batteries. Supercapacitors have nearly unlimited cyclibility (>100,000 cycles), low temperature dependence, and most importantly, enormously high power densities [5]. However, their energy density should be significantly improved to make them competitive in applications, where batteries are currently used. Optimization of the electrode material is the key step to increasing both gravimetric and volumetric capacitance of the supercapacitors.

Though supercapacitors employing metal oxides [6,7] or conducting polymers [8–10] have been increasingly investigated, carbon–carbon supercapacitors remain the most extensively studied and least expensive technology. Various carbonaceous materials such as activated carbons [11], aerogels [12], xerogels [13], templated carbons [14,15], nanotubes [16,17], and more recently carbide derived carbons (CDCs) [18–20], have been studied extensively as electrodes for supercapacitors. All of these carbons, with the exception of CDC, offer limited control over porosity. Furthermore, xerogels and many other carbons

* Corresponding author. Tel.: +1 215 895 6446; fax: +1 215 895 1934.
E-mail address: gogotsi@drexel.edu (Y. Gogotsi).

0378-7753/$ – see front matter © 2005 Elsevier B.V. All rights reserved.
doi:10.1016/j.jpowsour.2005.09.008

with high SSA have a very low density, which leads to a low volumetric capacitance and limits their practical use.

CDCs are obtained by selective leaching of metals from metal carbides with halogens in an elevated temperature environment [21,22]. The resulting carbon has high specific surface area (SSA), with pore sizes that can be fine-tuned by controlling the chlorination temperature [23] and by the choice of starting carbide [21,24]. They typically have a pore volume of 55–80%, depending on the carbide used and the synthesis conditions, with all pores open. Unlike templated carbons that use nanostructured silica as a sacrificial template and hydrofluoric acid to remove the template, CDCs can be produced in a closed process that is highly amenable to industrial size processing [24]. Previous work on Ti_3SiC_2 derived CDC showed very precise control of size [23]. B_4C and Ti_2AlC derived CDCs showed high specific capacitance [20] in H_2SO_4. Impressive results were also obtained in nonaqueous electrolytes [26], but no systematic study on effect of CDC synthesis conditions and resulting changes in pore size and specific surface area on performance in either aqueous or non-aqueous electrolytes has been reported.

As CDC allows precise tuning of the microstructure, porosity and functionality of the resulting porous carbon, it provides a good model system to study the effect of different properties on the electrochemical behavior of carbon in supercapacitors. This paper shows the strong correlation between micropores in ZrC and TiC derived CDC on both specific capacitance and frequency response in a sulfuric acid electrolyte.

2. Experimental

ZrC and TiC powders were treated with chlorine (Airgas, 95%) for 3 h at 600, 800, 1000, and 1200 °C in a horizontal quartz tube furnace. The internal reaction area that housed the carbide was isolated from the environment to prevent reaction with atmospheric gasses, allowing elimination of oxygen and hydrogen containing functional groups present in activated carbon samples prepared by other methods. Argon gas (Airgas, 99.998%) was flushed during heating and cooling of the furnace to purge atmospheric gas and atoms sorbed to the reaction area and carbide surfaces in the former case and to remove metal chlorides and unreacted chlorine in the latter. Exact details of the chlorination technique have been reported previously [27,28,31].

High-resolution transmission electron microscopy (HRTEM) was used to observe the CDC structure. The TEM samples were prepared by a 15-min sonication of the CDC powder in isopropanol and deposition on a lacy-carbon coated copper grid (200 mesh). A field-emission TEM (JEOL 2010F) with an imaging filter (Gatan GIF) was used at 200 kV.

Porosity analysis was carried out on CDC powders at −195.8 °C using a Quantachrome Autosorb-1 and argon as the adsorbate. Prior to analysis, samples were outgassed at 300 °C under vacuum for approximately 24 h. Pore size distributions were calculated from argon adsorption isotherms taken from a pressure range of 3×10^{-4} to 205 Torr using the non-local density functional theory (NLDFT) method provided by Quantachrome data reduction software version 1.27 assuming slit pore shape. SSA was calculated using both the Brunauer, Emmet, Teller (BET) method and the DFT method [25]. Most studies in literature attempt to correlate double-layer capacitance with total BET surface area, or in terms of micropore and mesopore surface area. Using DFT to calculate pore size distributions allows further comparison of double-layer capacitance with ultramicropores ($d < 1$ nm). Average pore size was determined by treating the DFT data statistically and fitting a non-linear log-normal function to it:

$$S = \frac{S_{\max}}{\sqrt{2\pi} w x} \mathrm{e}^{-[\ln(x/x_c)]^2/2w^2} \quad (1)$$

where, S is the differential surface area, x the pore size, x_c the pore size corresponding to the log-normal function maximum and the average pore size as defined in this study, $S_{\max}/\sqrt{2\pi} w x_c$ the maximum differential surface area, and w the parameter characterizing the width of the curve. The full width at half maximum (FWHM) of the pore-size distributions was calculated from the fitting curve (Eq. (1)) using the experimentally fitted parameters for w, x_c and $S_{\max}$.

The powders were processed into capacitor electrodes by mixing with 5 wt.% Teflon powder (E.I. du Pont de Nemours, Wilmington, DE), homogenized in a mortar and finally rolled into a thin film of uniform thickness (~175 μm). From this film, 1 cm^2 circular electrodes were punched out and pressed onto stainless steel mesh (200 mesh). As the volume of the electrodes was kept constant, the mass of CDC varied from 10 to 20 mg. Prior to testing, the electrodes were soaked in distilled water for 24 h to remove any chlorine not removed by heat treatment in argon. Subsequently, cleaned electrodes were inserted face to face against a porous polypropylene separator (Celgard Inc., Charlotte, NC), into a test cell with stainless steel current collectors, 1 M H_2SO_4 aqueous electrolyte and platinum wire as a quasi-reference electrode or in 2-electrode configuration, as noted. Cyclic voltammetry and impedance spectroscopy measurements were made using a Gamry PCI4/300 potentiostat.

Cyclic voltammetry tests were conducted at a scan rate of 5 mV s^{-1} within a window of −0.5 to 0.5 V in 2-electrode configuration. This voltage window was selected in order to remain far from the decomposition voltage of water and to avoid redox reactions between the current collectors and electrolyte. Specific capacitance was calculated directly from the CV using:

$$C = \frac{i}{sm} \quad (2)$$

where i is the instantaneous current, s the sweep rate and m the mass of the working electrode. Since capacitance is a function of voltage, it was averaged over the entire electrochemical window and over both the anodic and cathodic contributions.

Impedance measurements were conducted by applying a low-amplitude alternating voltage of 5 mV root mean square (RMS) to the system at its open cell voltage in a fully discharged state at frequencies from 10 kHz to 1 mHz. Considering the supercapacitor behaves as a series combination of a resistance, R, and capacitance, C, and both depend on frequency, ω, the impedance

can be written in complex form as:

$$Z = R(\omega) + \frac{1}{jC(\omega)\omega} \tag{3}$$

By taking into account the method used by Taberna et al. [30] to model impedance data, the total impedance is equated to a supercapacitance, K:

$$Z = R(\omega) + \frac{1}{jC(\omega)\omega} = \frac{1}{jK\omega} \tag{4}$$

leading to

$$K = \frac{C(\omega)}{1 + jR(\omega)C(\omega)\omega} = \frac{C(\omega)}{1 + R^2(\omega)C^2(\omega)\omega^2} - \frac{jC^2(\omega)R(\omega)\omega}{1 + R^2(\omega)C^2(\omega)\omega^2} \tag{5}$$

or

$$K = C' - jC'' \tag{6}$$

where C′ and –C″ are the real and imaginary components of supercapacitance, respectively:

$$C' = \frac{C(\omega)}{1 + R^2(\omega)C^2(\omega)\omega^2}; \quad C'' = \frac{C^2(\omega)R(\omega)\omega}{1 + R^2(\omega)C^2(\omega)\omega^2} \tag{7}$$

Alternatively, by considering the impedance in the complex form as:

$$Z(\omega) = Z'(\omega) + jZ''(\omega) \tag{8}$$

it is possible to derive the real and imaginary parts of supercapacitance directly from impedance data by using Eqs. (4) and (6):

$$C'(\omega) = \frac{-Z''(\omega)}{\omega|Z(\omega)|^2}; \quad C''(\omega) = \frac{Z'(\omega)}{\omega|Z(\omega)|^2} \tag{9}$$

$C'(\omega)$ corresponds to the capacitance of the cell measured under DC or low frequency AC conditions, while $C''(\omega)$ is directly proportional to resistance and corresponds to losses in the form of energy dispersion. Eqs. (7) and (9) allow the expression of capacitance both as a function of electrode properties and experimentally measured parameters.

3. Results

3.1. CDC structure

Previous work showed that ordering in CDC takes place over roughly three temperature regimes [27,28,31]: in the synthesis temperatures of 200–700 °C the CDC structure is largely amorphous, at ~800–1000 °C there is short-range structural ordering and above synthesis temperatures of 1100–1200 °C long range ordering (graphitization) begins to occur. These experimental results corroborate reverse Monte Carlo simulations on TiC-CDC by Zetterstrom et al. [32]. High resolution TEM analysis of TiC-CDC and ZrC-CDC show a logical progression of increasing order with increasing synthesis temperature occurring roughly in these temperature regimes (Fig. 1). At 600 °C, both TiC and ZrC-CDCs are amorphous (Fig. 1a and d). At 800 °C, the structures contain highly curved graphene planes (Fig. 1b and e). TiC-CDC produced at 800 °C has a higher content of fullerenic shell-type structures than ZrC-CDC synthesized at the same temperature and looked similar to the onion-like structures obtained by Zheng et al. [33]. For a synthesis temperature of 1200 °C (Fig. 1c and f), straight graphite fringes having interlayer spacing approaching that of pristine graphite

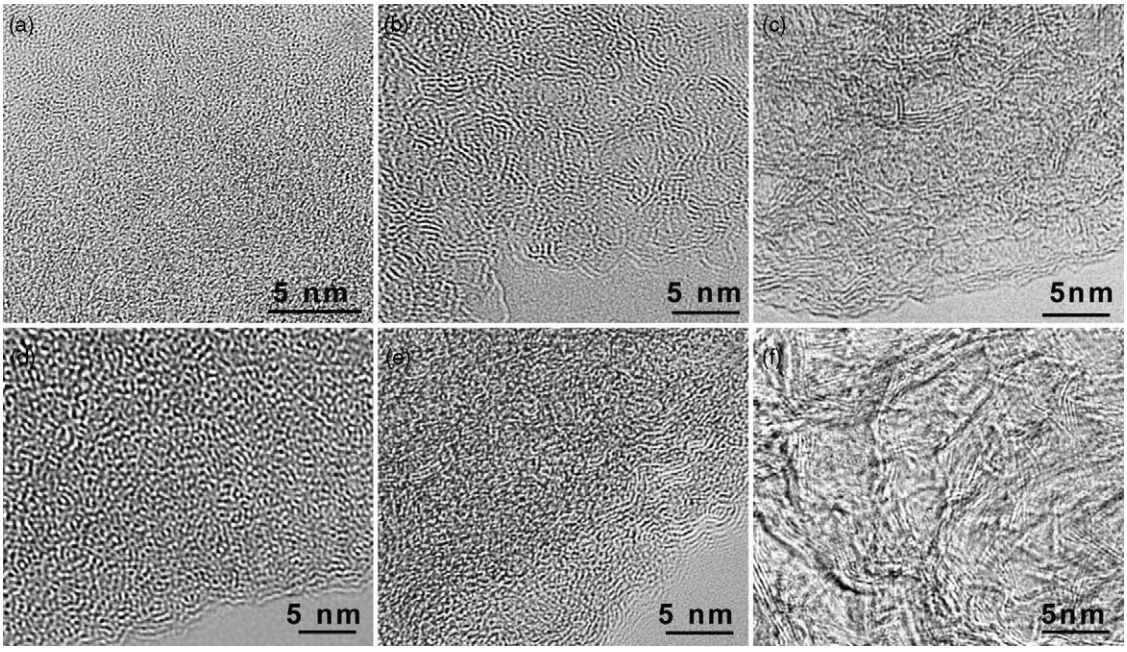

Fig. 1. TEM micrographs of TiC-CDC synthesized at (a) 600 °C, (b) 800 °C, (c) 1200 °C and ZrC-CDC synthesized at (d) 600 °C, (e) 800 °C, (f) 1200 °C.

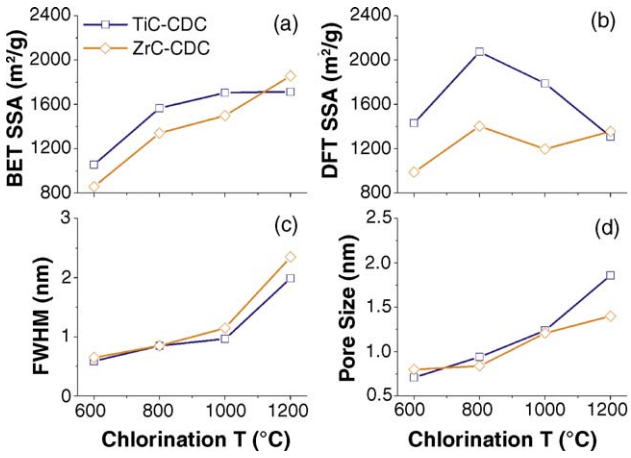

Fig. 2. Evolution of pore structure of TiC-CDC and ZrC-CDC with synthesis temperature. (a) BET specific surface area (SSA), (b) DFT SSA, (c) full width at half maximum (FWHM), and (d) average pore size.

(0.335 nm) are clearly visible. XRD study of these samples (data not shown) confirms the observed increase in graphitization at elevated temperatures.

TiC-CDC had a larger SSA than ZrC-CDC as calculated using both DFT and BET theory (Fig. 2a and b). Also, the BET SSA for both TiC-CDC and ZrC-CDC was found to increase with synthesis temperature (Fig. 2a), while the DFT SSA has a maximum at a synthesis temperature of 800 °C. Decrease of the DFT SSA at above 800 °C could be linked to the formation of multi-walled graphitic structures (Fig. 1c and f). The area between the walls in such structures should be not accessible to argon due to the small inter-wall spacing (as interplanar spacing in graphite). For TiC-CDC, the increase in BET SSA between synthesis temperatures of 800 and 1200 °C is small, but ZrC-CDC shows a near-constant increase over the entire range of synthesis temperatures studied.

Along with an SSA increase, ZrC and TiC-CDCs show a broadening pore size distribution with increasing synthesis temperature (Fig. 2c) as ordering opens up larger pores. This shifts the average pore size to larger values (Fig. 2d). Both TiC-CDC and ZrC-CDC have similar average pore size and FWHM (Fig. 2d and c) at a 600 °C synthesis temperature, 0.71 and 0.8 nm, respectively. At a synthesis temperature of 1200 °C, the average pore size for both CDCs differs more substantially. The FWHM calculated for both TiC-CDC and ZrC-CDC show the same development, with differences only in the average pore size. This highlights the ability of this class of carbon materials to have their pores fine-tuned [23].

Porosity and specific surface area growth follow similar ordering trends uncovered by TEM. At the lowest synthesis temperature, the amorphous structure is inundated with micropores. Since TiC and ZrC are isostructural, with differences only in lattice spacing, the initial spatial distribution of carbon atoms determines, to a limited extent, the final porosity of CDC. With increasing temperature, the individual carbon atoms are given more energy to migrate away from their initial spatial position in the carbide structure and to a more energetically favorable site, putting them in a metastable state between that of low synthesis temperature amorphous CDC and fullerenic structures. Increasing synthesis temperature moves this metastable state towards more graphitic structures and wider pores. Increasing the synthesis temperature from 600 to 800 °C creates new micropores, but at synthesis temperatures above this, the increase in surface area is a result of pores larger than 2 nm and comes at the expense of smaller micropores. This growth of mesopore SSA at the expense of micropore SSA is shown in Figs. 2 and 5.

3.2. Electrochemical measurements

Cyclic voltammetry tests showed the absence of any major faradic charge transfer, which would show up as peaks on either the cathodic or anodic side of the *I–V* loop (Fig. 3). From Fig. 3, it is also evident that as the synthesis temperature increases, the shape of the *I–V* loop becomes more rectangular, highlighting the decreasing equivalent series resistance with increasing synthesis temperature. Also apparent is the maximum in gravimetric specific capacitance ($F\,g^{-1}$) that occurs at a synthesis temperature of 800 °C (Fig. 3b) for both TiC- and ZrC-CDCs.

The gravimetric specific capacitance ($F\,g^{-1}$) for TiC- and ZrC-CDCs increases substantially from 108 and 81.5 $F\,g^{-1}$, respectively, to 190 and 159 $F\,g^{-1}$ between synthesis temperatures of 600 and 800 °C (Fig. 4a). Tests of TiC-CDC produced at 800 °C that was subsequently purified lead to even higher values of 208 $F\,g^{-1}$. These values are close to the upper limit reported by other groups [1,3] but stay within the range, showing the amenability of CDC to act as a model system for all porous carbons. The volumetric capacitance (VC) of TiC-CDC and ZrC-CDC were a maximum of 140 and 110 $F\,cm^{-3}$ (Fig. 4d), showing the practical usefulness of CDC as the active material in supercapacitor electrodes.

Above synthesis temperatures of 800 °C, the gravimetric specific capacitance (GC) decreases, though the BET SSA continues to increase up to synthesis temperatures of at least 1200 °C (Fig. 2a). The DFT SSA correlates very well with the specific capacitance, however (Fig. 2b). Fig. 4a and b shows that the surface specific capacitance (SC, $F\,cm^{-2}$) also has a decreasing

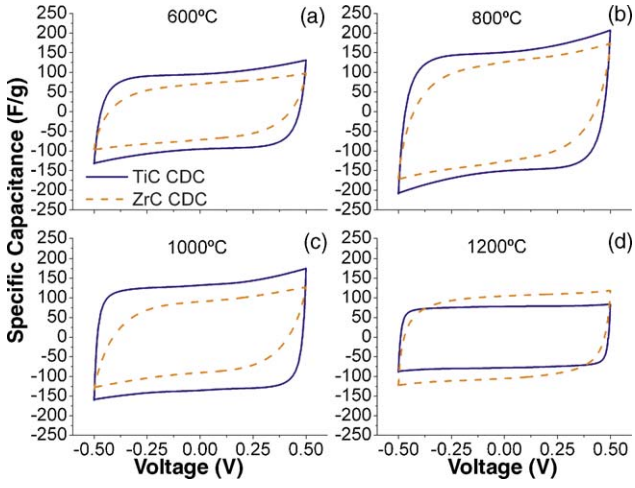

Fig. 3. Cyclic voltammograms taken at a scan rate of 5 mV/s of TiC-CDC and ZrC-CDC synthesized at (a) 600 °C, (b) 800 °C, (c) 1000 °C, and (d) 1200 °C.

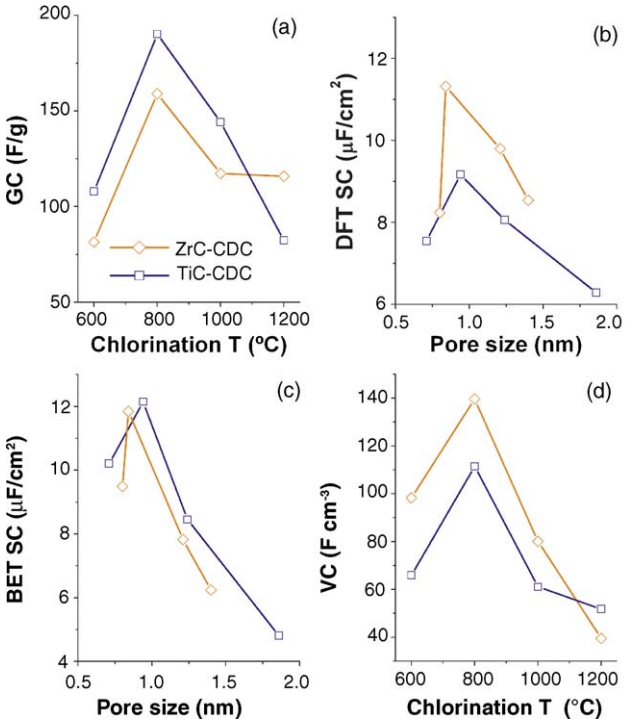

Fig. 4. (a) Specific gravimetric capacitance (GC) vs. chlorination temperature shows maximum capacitance at a synthesis temperature of 800 °C. Specific surface capacitance calculated using DFT SSA (DFT SC) (b) and BET SSA (BET SC) (c) vs. average pore size both show a decreasing trend with increasing pore size above 1 nm. (d) Volumetric capacitance (VC) shows a maximum at synthesis temperature of 800 °C.

trend with increasing pore size above 1 nm using both the DFT and BET criteria to calculate SSA.

From Fig. 3, it is evident that TiC-CDC has a larger specific capacitance than ZrC-CDC at all synthesis temperatures below 1200 °C. This is a direct result of the larger specific surface area of TiC-CDC in this temperature range.

Unlike most studies in literature that suggest increasing specific capacitance with increasing average pore size [34], this study shows a more complex behavior of porous carbons. Experiments on CDC demonstrate that decreasing the surface area of micropores serves to decrease both the gravimetric specific capacitance ($F\,g^{-1}$) and the specific surface capacitance ($F\,cm^{-2}$) in a sulfuric acid electrolyte (Fig. 5a and b). Even though the BET SSA continually grows with increasing synthesis temperature to the highest temperature studied, the specific capacitance decreases with decreasing micropore surface area at synthesis temperatures above 800 °C. These results corroborate those reported by Vix-Guterl et al. [35], which show that the non-solvated ions residing in pores smaller than 0.7 nm account for the largest portion of double-layer capacitance. Using DFT to calculate SSA shows that even though most of the area lies in smaller pores, it still remains highly accessible to electrolyte.

Shi suggested that specific capacitance calculated using galvanostatic charge–dischare and specific surface area calculated using gas sorption techniques are sufficient to gain precise understanding of how the pores of different sizes contribute to electrochemical performance [29]. This is a simple model that lumps

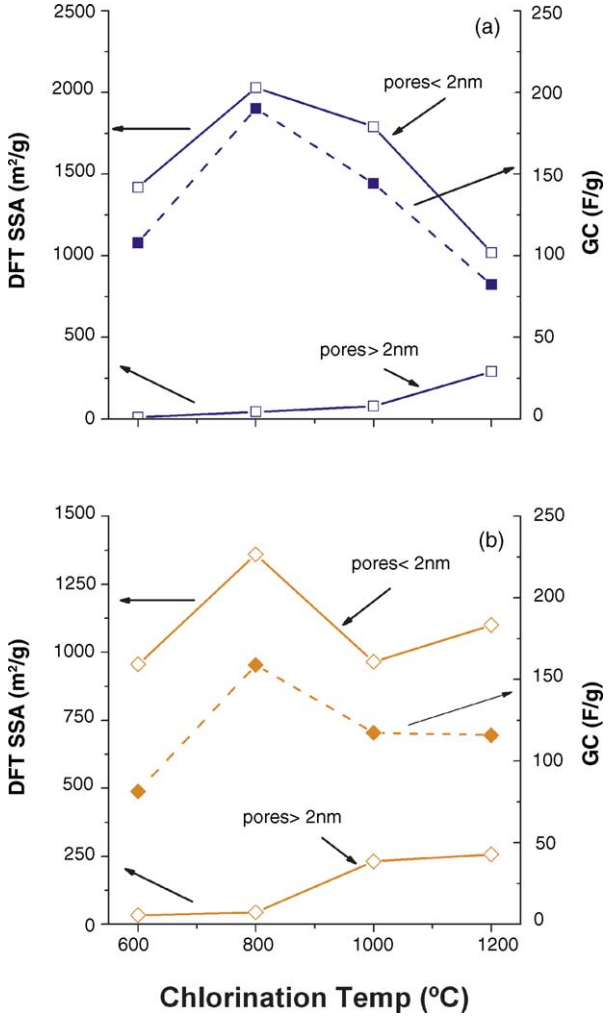

Fig. 5. Micropore (<2 nm) and mesopore (>2 nm) surface area in comparison with gravimetric specific capacitance for (a) TiC-CDC and (b) ZrC-CDC. A direct correlation between micropore surface area and specific capacitance is evident.

micropore and mesopore contributions to capacitance into two terms by assuming that pores larger than 2 nm have one fixed specific surface capacitance, C_{meso}, and pores smaller than 2 nm have another fixed specific surface capacitance, C_{micro}. The total specific capacitance is then simply:

$$C = S_{meso}C_{meso} + S_{micro}C_{micro} \tag{10}$$

where S_{meso} and S_{micro} are the surface area contributions from pores larger than 2 nm and pores smaller than 2 nm, respectively. By plotting experimental data on S_{micro}/S_{meso} against C/S_{meso} and fitting the data with a straight line, Shi suggested obtaining C_{micro} and C_{meso} from the slope and y-intercept of this line [29], according to Eq. (10) normalized by S_{meso}:

$$\frac{C}{S_{meso}} = C_{meso} + C_{micro}\frac{S_{micro}}{S_{meso}} \tag{11}$$

Though this is a much-cited technique, we believe that this treatment is misleading. As S_{micro}/S_{meso} is a very large value in high surface area carbons, large variations in C_{meso} among various carbons appear to be hidden in the graph. In fact, if one

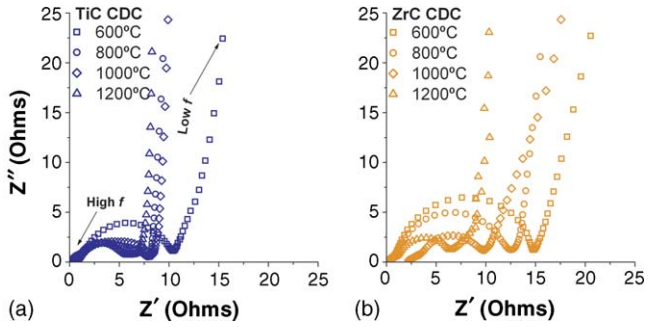

Fig. 6. Nyquist plots for (a) TiC-CDC and (b) ZrC-CDC synthesized at temperatures of 600, 800, 1000 and 1200 °C. The equivalent series resistance, which can be considered equal to the intersection of the low frequency region with the real axis is shown to decrease with increasing synthesis temperature.

plots S_{meso}/S_{micro} against C/S_{micro}, instead, no linear trend in the experimental graphs for CDC would be apparent (data not shown).

The effect of the mesopores/micropore ratio on complete device performance, including charge–discharge kinetics, could not be revealed by DC measurement techniques alone. To study the effect of frequency on the carbon electrodes, EIS was performed. Nyquist plots for TiC-CDC and ZrC-CDC synthesized at temperatures from 600 to 1200 °C (Fig. 6) show a decreasing equivalent series resistance, calculated as the intercept that the linear region makes with the real impedance axis, with increasing synthesis temperature. Also evident from Fig. 6 is the semi-circle that occurs at high frequencies. Portet et al. correlated this feature with poor conductivity between the current collector and carbon electrode [36]. ZrC-CDC has not been studied in literature, but the ESR for a TiC derived CDC sample in an acetonitrile-based electrolyte studied by Janes et al. [26] is less than 1 Ω, versus 12 Ω for 600 °C TiC-CDC in our experiments. It is expected that further refinement of the supercapacitor cell construction would significantly decrease the ESR to a value lower than this due to the higher ionic conductivity of water, eliminating the high frequency semi-circle and shifting the entire plot to lower values of real impedance. In the low frequency regime, capacitors assembled from CDCs synthesized at all temperatures show ideal capacitive behavior, with a near vertical line parallel to the imaginary axis.

Fig. 7a and b shows the evolution of $C'(\omega)$ normalized by $C'(1\,\text{mHz})$ versus frequency, according to Eqs. (5) and (7). This type of plot provides a convenient method to show the frequency response of supercapacitors because frequency is the dependant variable, unlike Nyquist plots that have frequency buried in both the real and imaginary impedance terms. The graph shows a transition between purely resistive behavior, where $C'(\omega)/C'(1\,\text{mHz})$ is equal to zero ($R^2C^2w^2 \gg 1$ in Eq. (7)) to purely capacitive behavior where $C'(\omega)/C'(1\,\text{mHz})$ is equal to 1 ($R^2C^2w^2 \ll 1$ in Eq. (7)). Ideally for applications, the capacitance should remain nearly invariant with frequency once this transition ($R^2C^2w^2 \sim 1$) is passed. TiC-CDC (Fig. 7a) synthesized at temperatures above 800 °C shows this ideal behavior, while for samples synthesized at lower temperatures, capacitance continues to increase with decreasing frequency. ZrC-CDC (Fig. 7b) shows ideal behavior for only the 1200 °C sample.

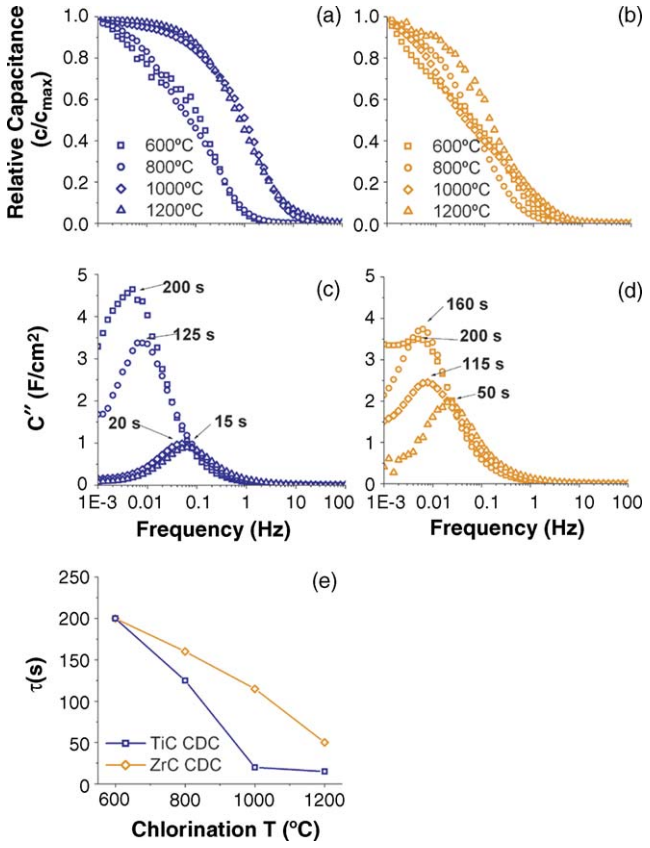

Fig. 7. Progression of the relative real capacitance, $C'(\omega)/C'(1\,\text{mHz})$ for (a) TiC-CDC and (b) ZrC-CDC, and the imaginary capacitance, $C'(\omega)$ for (c) TiC-CDC and (d) ZrC-CDC with frequency for synthesis temperatures of 600, 800, 1000 and 1200 °C shows dependence on synthesis temperature. (e) Variation of the characteristic time constant, τ, with synthesis temperature for TiC-CDC and ZrC-CDC.

Fig. 7c and d shows the evolution of the imaginary capacitance with frequency according to Eq. (7). The maximum of the curve is a characteristic of the entire system and can be roughly described as the point where the circuit goes from purely resistive to purely capacitive [30]. The frequency, f_0, where this maximum occurs shifts to higher values with increasing synthesis temperature (Fig. 7c and d). The reciprocal of the characteristic frequency yields a time constant, τ, that is a quantitative measure of how fast the device can be charged and discharged reversibly. For both CDCs, this time constant decreases with increasing synthesis temperature (Fig. 7e). Interestingly, for TiC-CDC there is a large decrease in τ between synthesis temperatures of 600 and 1000 °C and little change between 1000 and 1200 °C. ZrC-CDC has a uniform decrease of τ_0 with synthesis temperature. For 600 and 800 °C synthesis temperatures, the values for τ_0 match up pretty closely for both materials, but at higher synthesis temperatures, τ_0 decreases much more for TiC-CDC.

These results give valuable insight into the role of pore size on the frequency response of porous carbons. According to Eq. (7), there are two factors, $R(\omega)$ and $C(\omega)$, that determine the frequency response of both the real and imaginary capacitance. $R(\omega)$ can be assumed to be the sum of two contributions: a frequency independent term equal to the ESR and a frequency dependent term, $R_f(\omega)$, connected with inhibited ion motion in

small pores. As the pore structure has no influence over the ESR, the roles of increasing graphitization and increasing pore size on EIS results can be separated. For both TiC-CDC and ZrC-CDC, there is a decreasing ESR of approximately the same magnitude of ~100% from synthesis temperatures of 600 to 1200 °C. This can be directly related to the increasing graphitization with increasing synthesis temperature observed in all CDCs. From Fig. 7e, it is apparent that the characteristic time constants for samples synthesized at 600 and 1200 °C for TiC- and ZrC-CDCs decrease by approximately a factor of 12 and 3, respectively. As the decrease in time constant is greater than that of the ESR, it can be directly inferred that widening of the pores has a positive effect on the time constant.

The large difference between characteristic time constants for TiC-CDC and ZrC-CDC synthesized at 1000 and 1200 °C was surprising. As both materials have essentially the same ESR at both synthesis temperatures, explaining the result as a consequence of larger pores in TiC-CDC would seem the most plausible answer. Unfortunately, though the difference in pore sizes at 1200 °C synthesis temperatures is sufficient to make this rationalization conceivable, at a 1000 °C synthesis temperature, the average pore size and FWHM are very similar. The main difference in these two materials at these synthesis temperatures is then not the average pore sizes, but how easily accessible these pores are. Larger molecules of $ZrCl_4$ and its higher boiling point make removal of this chloride from pores more difficult during synthesis. Hydrolyzed $ZrCl_4$ also leaves some ZrO_2 in the pores, which may plug pore channels and decrease pore accessibility to electrolyte ions. This highlights the fact that basing expected supercapacitor performance simply on pore size measured by gas sorption is short sighted. Bottlenecks that may be present but not detectible by gas sorption could have major influence over the charging and discharging of supercapacitors. The discussed phenomenon creates an additional challenge to predict electrochemical performance of porous carbon materials based on their physical characteristics. Additional sorption tests with larger molecules, such as SF_6, may be a way to circumvent this problem.

4. Conclusions

Specific capacitance was shown to closely mirror the development of micropore surface area for both TiC-CDC and ZrC-CDC and reached a maximum of 190 F g^{-1} and 150 F g^{-3} at a synthesis temperature of 800 °C. Volumetric capacitance was also a maximum at 800 °C and was 110 and 140 F cm^{-3} for ZrC- and TiC-CDCs. Increasing the volume of pores smaller than 2 nm was shown to increase specific capacitance, while increasing the volume of pores larger than 2 nm at the expense of smaller pores had a detrimental effect on specific capacitance. Pores with a size of 0.8–1 nm lead to the highest specific surface capacitance (F cm^{-2}) in 1 M H_2SO_4. Increasing synthesis temperature increased the average pore size, which had a positive effect on both the characteristic time constant and the ESR for both types of carbon materials studied. Pore convolution, not detectible by standard gas sorption techniques, may have a strong influence on frequency response of supercapacitors and increases the difficulty in screening carbons for supercapacitor applications using gas sorption alone.

Acknowledgements

This work was supported by Arkema, France. We are very grateful to Dr. John E. Fischer at the University of Pennsylvania for providing us electrochemical cells and numerous propitious discussions. HRTEM was performed at the Penn Regional Nanotechnology Facility at the University of Pennsylvania.

References

[1] F. Beguin, Carbon 39 (2001) 937–950.
[2] R. Kotz, M. Carlen, Electrochim. Acta 45 (2000) 2483–2498.
[3] A. Burke, J. Power Sources 91 (2000) 37–50.
[4] H.E. Becker, Low voltage electrolytic capacitor, US Patent 2,800,616 (1957).
[5] B.E. Conway, Electrochemical Capacitors: Scientific Fundamentals and Technological Applications, Kluwer, 1999.
[6] B.E. Conway, V. Birss, J. Wojtowicz, J. Power Sources 66 (1997) 1–14.
[7] J. Jiang, A. Kucernak, Electrochim. Acta 47 (2002) 2381–2386.
[8] C. Arbizzani, M. Mastragostino, L. Meneghello, R. Paraventi, Adv. Mater. 8 (1996) 331–334.
[9] J.C. Lassegues, J. Grondin, T. Becker, L. Servant, M. Hernandez, Solid State Ionics Diffus. React. 77 (1995) 311–317.
[10] M. Mastragostino, C. Arbizzani, F. Soavi, J. Power Sources 97–98 (2001) 812–815.
[11] M. Endo, Y.J. Kim, K. Osawa, K. Ishii, T. Inoue, T. Nomura, N. Miyashita, M.S. Dresselhaus, Electrochem. Solid State Lett. 6 (2003) A23–A26.
[12] R. Saliger, U. Fischer, C. Herta, J. Fricke, J. Non-Cryst. Solids 225 (1998) 81–85.
[13] C. Lin, J.A. Ritter, B.N. Popov, J. Electrochem. Soc. 146 (1999) 3639–3643.
[14] A. Huczko, Appl. Phys. A 70 (2000) 365–376.
[15] A.B. Fuertes, F. Pico, J.M. Rojo, J. Power Sources 133 (2004) 329–336.
[16] E. Frackowiak, S. Delpeux, K. Jurewicz, K. Szostak, D. Cazorla-Amoros, F. Beguin, Chem. Phys. Lett. 361 (2002) 35–41.
[17] E. Frackowiak, K. Jurewicz, S. Depleux, F. Beguin, J. Power Sources 97–98 (2001) 822–825.
[18] E. Lust, A. Janes, M. Arulepp, J. Electroanal. Chem. 562 (2003) 33–42.
[19] E. Lust, G. Nurk, A. Janes, M. Arulepp, L. Permann, P. Nigu, P. Moller, Condens. Matter Phys. 5 (2002) 307–327.
[20] J. Chmiola, G. Yushin, R.K. Dash, E.N. Hoffman, J.E. Fischer, M.W. Barsoum, Y. Gogotsi, Electrochem. Solid State Lett. 8 (2005) A357–A360.
[21] A. Nikitin, Y. Gogotsi, in: H.S. Nalwa (Ed.), Encyclopedia of Nanoscience and Nanotechnology, vol. 7, Amer. Sci. Publ., 2004, pp. 553–574.
[22] Y. Gogotsi, J.-D. Jeon, M.J. McNallan, J. Mater. Chem. 7 (1997) 1841–1848.
[23] Y. Gogotsi, A. Nikitin, H. Ye, W. Zhou, J.E. Fischer, B. Yi, H.C. Foley, M.W. Barsoum, Nat. Mater. 2 (2003) 591–594.
[24] G. Yushin, A. Nikitin, Y. Gogotsi (Eds.), Handbook of Nanomaterials, CRC Press, 2005, in press.
[25] P.I. Ravikovitch, A. Neimark, Colloid Surface A 187–188 (2001) 11–21.
[26] A. Janes, L. Permann, M. Arulepp, E. Lust, Electrochem. Commun. 6 (2004) 313–318.
[27] R.K. Dash, G. Yushin, Y. Gogotsi, Mircopor. Mesopor. Mater. 86 (2005) 50–57.
[28] R.K. Dash, J. Chmiola, G. Yushin, Y. Gogotsi, G. Laudisio, J. Singer, J. Fischer, S.O. Kucheyev, Carbon (2006), in press.
[29] H. Shi, Electrochim. Acta 41 (1996) 1633–1639.
[30] P.L. Taberna, P. Simon, J.F. Fauvarque, J. Electrochem. Soc. 150 (2003) A292–A300.

[31] R.K. Dash, A. Nikitin, Y. Gogotsi, Mircopor. Mesopor. Mater. 72 (2004) 203–208.
[32] P. Zetterstrom, S. Urbonaite, F. Lindberg, R.G. Delaplane, J. Leis, G. Svensson, J. Phys.: Condens. Matter. 17 (2005) 3509–3524.
[33] J. Zheng, T.C. Ekström, S.K. Gordeev, M. Jacob, J. Mater. Chem. 10 (2000) 1039–1041.
[34] F. Beck, M. Dolata, E. Grivei, N. Probst, J. Appl. Electrochem. 31 (2001) 845–853.
[35] C. Vix-Guterl, E. Frackowiak, K. Jurewicz, M. Friebe, J. Parmentier, F. Beguin, Carbon 43 (2005) 1293–1302.
[36] C. Portet, P.L. Taberna, P. Simon, C. Laberty-Robert, Electrochim. Acta 49 (2004) 905–912.